

PACS numbers: 87.64.Cc; 07.60.Vg
DOI: 10.1070/QE2010v040n12ABEH014503

Non-invasive, MRI-compatible fibreoptic device for functional near-IR reflectometry of human brain

H.S.S. Sorvoja, T.S. Myllylä, M.Yu. Kirillin, E.A. Sergeeva, R.A. Myllylä, A.A. Elseoud, J. Nikkinen, O.Tervonen, V. Kiviniemi

***Abstract*. A non-invasive device for measuring blood oxygen variations in human brain is designed, implemented, and tested for MRI compatibility. The device is based on principles of near-IR reflectometry; power LEDs serve as sources of probing radiation delivered to patient skin surface through optical fibres. Numerical Monte Carlo simulations of probing radiation propagation in a multilayer brain model are performed to evaluate signal levels at different source – detector separations at three operation wavelengths and an additional wavelength of 915 nm. It is shown that the device can be applied for brain activity studies using power LEDs operating at 830 and 915 nm, while employment of wavelength of 660 nm requires an increased probing power. Employment of the wavelength of 592 nm in the current configuration is unreasonable.**

Keywords: *near-IR reflectometry, brain activity, Monte Carlo simulations, MRI, power LED, lock-in amplifier.*

1. Introduction

Due to its non-invasiveness and safety, functional magnetic resonance imaging (fMRI) has become a major tool in the investigation of brain activity. The functional magnetic resonance imaging of the task activation-related blood flow has greatly increased the knowledge of brain functionality during the past two decades since the pioneering work of Ogawa et al. [1]. Recently, the focus of interest has been on detecting and modelling spontaneous fluctuations in brain activity, initially discovered by Biswal et al. [2]. Although the presence of these very low frequency fluctuations has been known for over a decade now, their origin is still largely unexplained. Kiviniemi [3] has proposed that these connectivity fluctuations arise from several sources, namely, electrophysiological, metabolic, and vascular ones. To specify the origin of these fluctuations, optical diagnostic techniques sensitive to blood oxygenation parameters can be applied simultaneously with fMRI.

Figure 1 presents absorption spectra for oxyhemoglobin and deoxyhemoglobin, the two principal chromophores in human tissue, from the visible to the near-IR region [4]. Blood oxygen variations can be determined by measuring reflected probing radiation at two or more wavelengths chosen at different sides from the isobestic point near 800 nm [5]. Interesting wavelengths in this respect are 600 – 750 nm and 800 – 900 nm. In addition, Vern et al. [6] used 590 nm to measure slow oscillations in the cortical blood volume of rabbits.

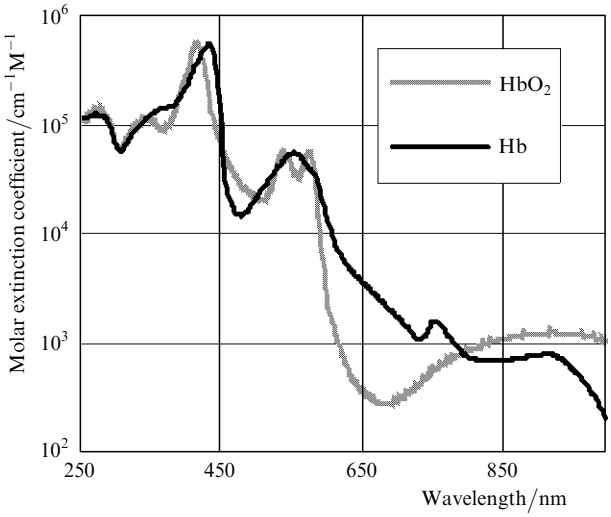

Figure 1. Absorption spectra for oxyhemoglobin and deoxyhemoglobin [4].

Existing commercially available and experimental devices for near-IR spectroscopy and tomography of brain [7] can be divided into several categories in accordance with the operation principles: continuous wave spectroscopy (CWS), spatially resolved spectroscopy (SRS), time resolved spectroscopy (TRS), phase modulation spectroscopy (PMS), and diffusing-wave spectroscopy (DWS). Commercially available devices are often based on either the CWS or the PMS techniques. The CWS devices tend to use two or more wavelengths in the multiplexed regime. They are relatively cheap; however, the price depends on the number of the

H.S.S. Sorvoja, T.S. Myllylä, R.A. Myllylä University of Oulu, Optoelectronics and Measurement Techniques Laboratory, P.O. Box 4500, 90014, Oulu, Finland; e-mail: risto.myllyla@ee.oulu.fi;
M.Yu. Kirillin, E.A. Sergeeva Institute of Applied Physics, Russian Academy of Sciences, ul. Ul'yanova 46, Nizhnii Novgorod, Russia; e-mail: mkirillin@yandex.ru;
A.A. Elseoud, J. Nikkinen, O.Tervonen, V. Kiviniemi MRI Research Unit, Department of Diagnostic Radiology, Oulu University Hospital, P.O. Box 50, 90029, Oulu, Finland; juha.nikkinen@oulu.fi

Received 28 October 2010
Kvantovaya Elektronika **40** (12) 1067 – 1073 (2010)
Submitted in English

used wavelengths and channels. The PMS, TRS, and SRS devices, on the other hand, are much more complex systems, usually applying one or more lasers in combination with temperature control systems and a sophisticated system for detecting reflected optical signals.

The aim of the present work is to develop an fMRI-compatible NIRS (near infrared spectroscopy) system capable of measuring blood oxygen variations with simultaneous fMRI, electro-encephalography (EEG), and non-invasive blood pressure (NIBP) measurements. An NIBP device has been designed and constructed in the Optoelectronic and Measurement Techniques Laboratory of the University of Oulu [8] for radiology studies. The ultimate goal of NIRS, fMRI, EEG, and NIBP simultaneous measurements is detection and quantification of mutual dependence of corresponding characteristics [2, 3]. Understanding the relationship between the known sources of fluctuations, i.e., electrophysiological, metabolic, and vascular ones, is a prerequisite for utilising the system in a clinical setting [3]. The paper also discusses efficiency and MRI-compatibility of the developed device.

2. MRI compatibility requirements

NIRS system performance simultaneously with MR-imaging environment poses high demands to it, as it cannot contain any ferromagnetic materials, which would be affected by the strong magnetic fields generated by the MRI scanner. All the used materials should be MR-compatible, including such metals as aluminium, zinc, titan, copper, and brass [9] as well as most types of plastic, silica and, for example, wood. Unfortunately, the pins and leads of integrated circuits and discreet components and screws may contain ferromagnetic materials; however, their non-significant presence is acceptable provided that the device is placed outside a 2 mT ring around the MRI scanner (indicated as outer dasher radius in Fig. 2).

In addition, the devices must be electromagnetically sealed to prevent any mutual influence of electromagnetic fields of NIRS system and MR-scanner. The technologic holes in the device enclosure must be not larger than approximately 3 cm in diameter providing effective shielding from MHz radiation, while GHz radiation do not affect the quality of MR-images [10].

3. Monte Carlo simulation of brain functional near-IR reflectometry

To simulate the operation of the constructed device before actual measurements and to evaluate the required probing power and detector sensitivity, we developed a Monte Carlo code for simulating light transport within a multilayer model mimicking the human head. The code is based on the previously developed code described in [11, 12], where it was used to simulate glucose sensing in a multilayer biotissue phantom. We employed planar geometry of the layers previously introduced by Okada [13]. Table 1 presents the optical and geometrical properties of the layers used in simulations [14–18].

The calculations were performed at four different wavelengths, three of which correspond to the operating wavelengths of the constructed device (592, 660, and 830 nm), while the fourth one (915 nm) is an additional wavelength, which could be added to the device in the future. For each calculation, we launched 10^8 photons. Having a radius of 1.5 mm, the probing beam was considered to be round in shape with a flat intensity distribution, and the detection numerical aperture was chosen as 0.6, corresponding to the setup parameter. The radial distribution of backscattered intensity was calculated to allow estimating the signal level at different source–detector separation distances.

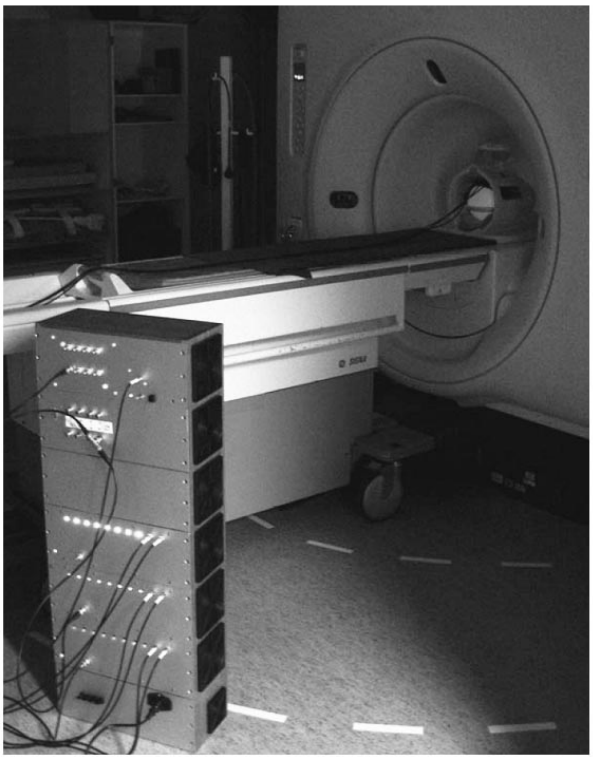

Figure 2. NIRS system (left) in the MRI-compatibility experiment. The calibration phantom is inside the MR-scanner. White dashed lines indicate magnetic field levels. Outer radius corresponds to 2 mT.

4. Experimental setup

In our NIRS system we used power LEDs as probing radiation sources which is more budget solution compared to a multi-channel laser diode measurement system with thermal controllers in each laser driver. The constructed device comprised four power LED drivers, each with 10 separately controllable channels, a programmable 8-channel function generator, a four channel lock-in amplifier block, data acquisition block, and a microcontroller-based measurement control block (Fig. 3). The system is controlled by a computer with LabView software situated outside the MRI-room. All of these printed circuit boards (PCBs) were designed and constructed at the Optoelectronics and Measurement Techniques Laboratory.

A set of ten 7-metre fibre bundles (one per each LED driver channel) were used to deliver light on the patient's skin on the head. Each bundle consists of 4 fibres for delivering radiation from 4 power LEDs. The diameter of a probing fibre is 1.25 mm. All the bundles were constructed to have a 90 degree curvature at the patient end; this requirement is caused by the design of the 'helmet' which the patient wears inside the MRI scanner, enabling the fibre

Table 1. Optical properties of biotissues within the human head at various wavelengths (592/660/830/915 nm).

Tissue	Layer thickness L/mm	Scattering coefficient μ_s/mm^{-1}	Absorption coefficient μ_a/mm^{-1}	Anisotropy factor g	References
Scalp	3	25/20/15/12	0.07/0.06/0.05/0.05	0.81/0.82/0.86/0.88	[14, 15]
Skull	10	38/36/28/25	0.065/0.035/0.025/0.04	0.92/0.925/0.94/0.94	[16]
Cerebrospinal fluid (CSF)	2	0.1	0.001	0.999	[13]
Gray matter	4	60/60/60/60	0.15/0.05/0.03/0.03	0.95/0.95/0.96/0.96	[17]
White matter	20	45/50/55/60	0.08/0.02/0.01/0.01	0.78/0.8/0.85/0.87	[18]

bundles to be led along the skin surface. The probing fibre bundles are situated around the central receiving fibre. All the bundles had a soft silicon rubber jacket. The receiving fibre serves for delivery of scattered probing radiation to preamplifier and photodiode; its diameter is 2.75 mm. The voltage signal is then amplified and read by a data acquisition card.

All devices were shielded by separate aluminium boxes, assembled on a rack made of MDF (medium density fibre). Because the LED drivers require a massive heat sink at the back of the box, the cooling of the power LEDs and driving power circuits was carefully organised. Due to usage of fans the thermal resistance of the heat sinks was reduced from about 1 K W^{-1} to less than about 0.1 K W^{-1}.

4.1 Sources of probing radiation

Several power LED types were studied, and we chose LEDs on an aluminium plate with a thread, which were supposed to have high thermal conductance (Roithner, M3L series, 660 nm and 830 nm). The plastic lenses of the LEDs were removed and an SMA-905 connector was attached exactly on the open silicon chip, leaving a gap of only 0.1 mm. This arrangement allowed bringing maximum optical power into the fibre bundle. The yellow 592 nm LED (Lumex LX1610SYC) has a maximum throughput of about 14 mW of optical power. Since optical power is a linear function of current only up to about 200 mA, the maximum usable output power of this LED is only 8 mW (Fig. 4). In the linear range, the maximal output powers of the other LEDs are 25 mW for 660 nm and 7 mW for 830 nm. The default probing power corresponds to half the power of the linear output range.

4.2 Modulation

To achieve a high signal-to-noise ratio, coherent detection, i.e., lock-in amplification, must be used, as it enables background light suppression, noise reduction, and wavelength-encoding for the different LEDs. Encoding means that the different colours of LEDs are amplitude modulated by different frequencies, allowing the colours to be distinguished from each other. To accomplish modulation, a programmable function generator produces four perfectly

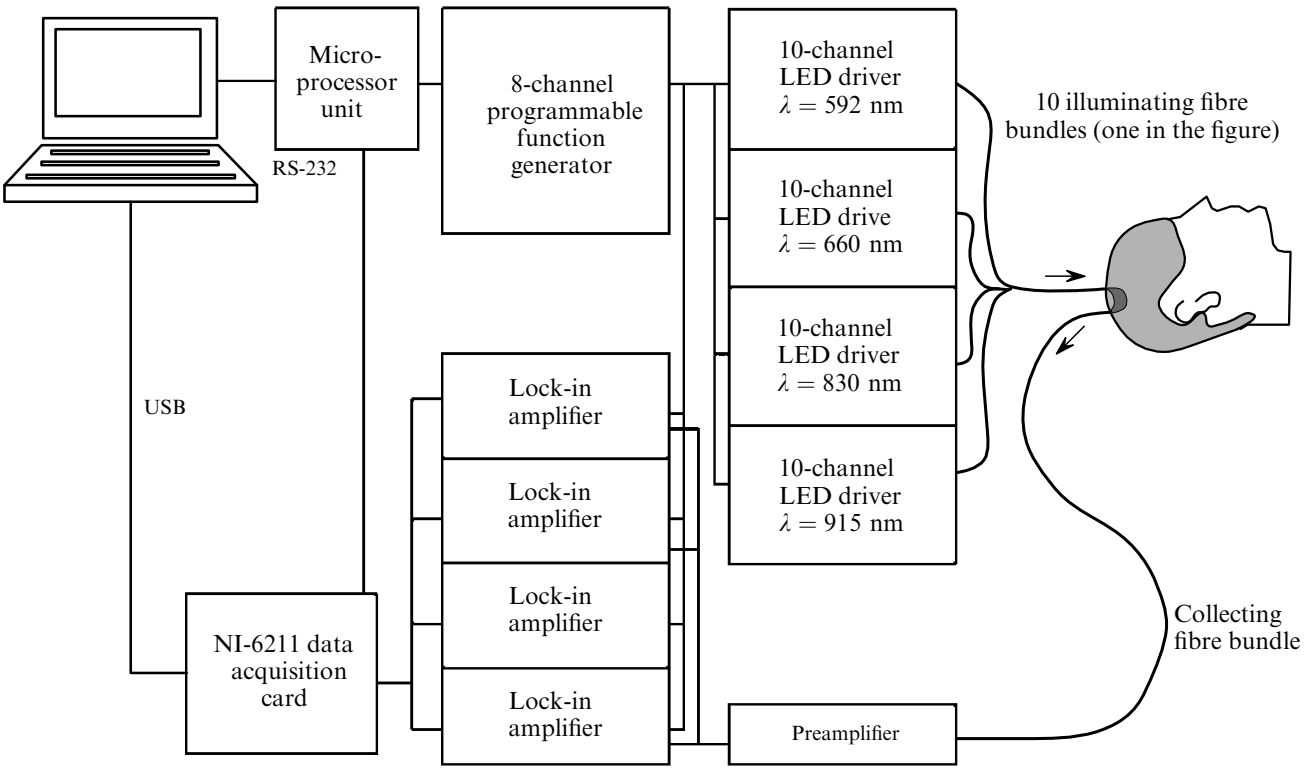

Figure 3. Block diagram of the NIRS system.

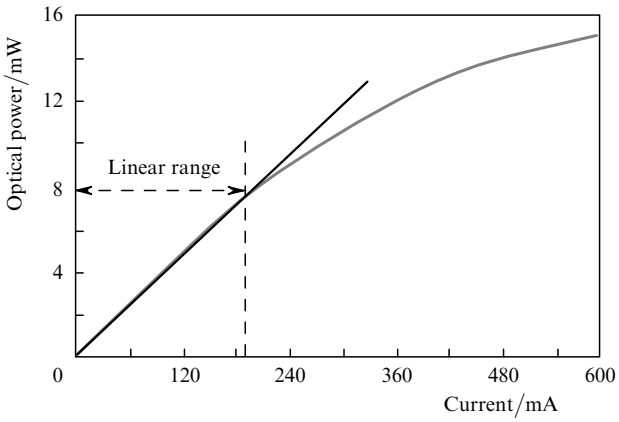

Figure 4. Optical output power of a Lumex LX1610SYC LED as a function of current. Half the power is achieved with current of 100 mA.

sinusoidal waveforms of up to 12 MHz and modulation coefficient of 1. The lock-in amplifiers for different wavelength are clocked by the corresponding frequencies.

4.3 Receiver

The lower limits of the receiver's light detection capacity are determined by its noise characteristics. Noise is generated by the shot noise of the background light and the thermal and shot noise of the photodiode and amplifier circuit of the receiver. Designing a receiver circuit typically involves a trade-off between speed vs. sensitivity and noise. As a consequence, the response speed of the photodiode can be increased by applying a bias voltage to it. Unfortunately, this also serves to increase both thermal and shot noise.

According to its datasheet, the S2386-18K photodiode [19] has a rise time of 0.4 μs, if the reverse voltage is 0 V. Thus, when using an unbiased detector circuit, the cut-off frequency of the photodiode is 875 kHz, which limits the frequency to be sampled to below 437.5 kHz. However, in this application, the amplitude modulation frequency can be rather low, below the calculated limit. Therefore, it is possible to utilise an unbiased photodiode circuit to minimise noise. The noise equivalent power (NEP) of the S2386-18K photodiode, when unbiased, is 6.8×10^{-16} W Hz$^{-1/2}$, while its effective active area is 1.2 mm^2.

Since photodiodes tend to produce less noise than amplifiers, the detector's response level is also highly dependent on the amplifier circuit. In the developed NIRS system we use a transimpedance op-amp, because its simple topology has smaller noise sources. Figure 5 shows the equivalent noise circuit of the photodiode and transimpedance circuit, representing noise sources as current noise generators. It is assumed that the output resistance of the operational amplifier is less than R_f and R_{sh}. Moreover, if the first stage is properly designed, the signal-to-noise ratio is unaffected by the second stage voltage amplifier [20]. Total noise I_n^{tot} is computed as the square root of the sum of the squares of the individual noise types.

$$I_n^{tot} = (I_{sn}^2 + I_{jn}^2 + I_n^2 + I_{n,e}^2 + I_f^2)^{1/2}, \quad (1)$$

where I_{sn} is the shot noise; I_{jn} is the junction noise; I_d is the dark current; I_f is the feedback current; I_n is the amplifier current noise; $I_{n,e}$ is the amplifier voltage noise.

The amplifier current noise and thermal noise from the feedback resistor R_f can be calculated as

$$I_n = i_n\sqrt{B}, \quad I_f = \left(\frac{4kTB}{R_f}\right)^{1/2}, \quad (2)$$

In equation (2), B is the bandwidth; $k = 1.381 \times 10^{23}$ J K^{-1} is Boltzmann's constant; T is temperature. The noise from R_f becomes minor, if its value is sufficiently large.

Besides the photodiode, most of the noise present is generated by the amplifier, if the feedback resistor and capacitor values are properly chosen.

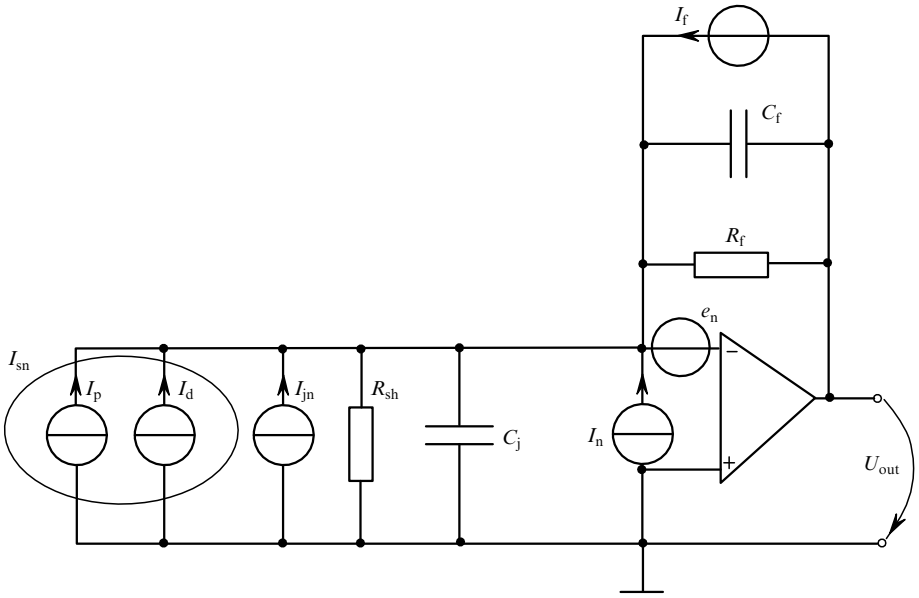

Figure 5. Equivalent detector and transimpedance operational amplifier circuit with its noise sources (R_f is the feedback resistor, R_{sh} is the shunt resistor, C_f is the feedback capacitor, C_j is the junction capacitor, I_d is the dark current, I_p is the photocurrent; e_n is the amplifier voltage noise, U_{out} is the output voltage).

$$I_n^{tot} \approx (I_n^2 + I_{n,e}^2)^{1/2}, \quad (3)$$

$$I_{ne} = e_n \frac{R_{sh} + R_f}{R_{sh} R_f} \sqrt{B}. \quad (4)$$

For the chosen ultralow noise op-amp such as LMH6624 from National Semiconductor, the amplifier voltage noise e_n is 0.92 nV $Hz^{-1/2}$ and the amplifier current noise i_n is 2.3 pA $Hz^{-1/2}$.

The signal current-to-noise-current ratio is determined by

$$SNR = I_s / I_n^{tot}, \quad (5)$$

where I_s is the signal current of the photodiode which is calculated with expression $I_s = P\eta$ (η is the photosensitivity and P is input power). For wavelengths between 590 nm and 900 nm, the photosensitivity η of the S2386-18K photodiode varies between 0.4 and 0.6 A W^{-1}.

By using lock-in amplification technique, it is possible to minimise noise due to very narrow bandwidth (typically 1–10 mHz). Table 2 presents the threshold dependence of different bandwidths when $R_f = 10$ MΩ and $R_{sh} = 100$ GΩ when using an LMH6624 op-amp and S2386-18K photodiode.

Table 2. Bandwidth dependence of the detector threshold.

Bandwidth/Hz	Threshold/pW
0.001	0.18
0.01	0.58
0.1	1.82
1	5.8
10	18.8
100	57.5

5. Results and discussion

5.1 MRI-compartibility

To study MRI-compatibility of the developed device, we performed a series of experiments of MR-imaging of the test object in presence of the constructed NIRS system. The measurements showed that the materials of the device did not introduce noise into MR images, when placed outside the 2 mT zone, marked as an outer white circle in Figure 2.

Thus, selected materials including MDF in the enclosure, aluminium in the front panels and device boxes, and brass in the screws provide MRI-compatibility of the NIRS system. On the other hand, our preliminary tests showed that even a weak electrical current in the fan cables produced blurring of the MR image when the cables were not sealed separately. Using the test setup we tested a poorly shielded LED driver and a similar, better shielded driver, both installed on the devise rack, but switched on separately. Figures 6a–c present three MR images of a calibration phantom. Figure 6a shows an undisturbed reference MR image versus Figs 6b and 6c depicting disturbed images of the same calibration phantom with turned on unshielded and shielded LEDs correspondingly. As seen from Fig. 6c, the quality of the MR image improved significantly when the better shielded LED driver was turned on.

5.2 Probing optical power measurements

Measured separately, the output optical power of each LED was determined using ten channels for yellow, red, and IR. Measured from the connector and the fibre bundle, mean output power values are presented in Table 3.

Table 3. Average LED output power when calibrated at half the power in the linear range.

Wavelength/nm	Average output power measured from the LED's output connector/mW	Power measured from the output of the fibre bundle/mW
592	0.83	1.04
660	1.16	1.22
830	2.61	1.98

The reason for the larger optical power readings obtained from the output of the fibre bundle than from the SMA-905 connector with a LED at 592 nm is that the fibre bundle is attached almost in contact with the LED chip surface, whereas the connector hole and the chip surface of the SMA-905 have a gap between them. As a result, the fibre bundle gathers a larger amount of submitted power than the connector's hole. According to Fig. 4, half the power output at a current of 100 mA yields about 4 mW, with a yellow LED, however, only about 1 mW can be measured from the connector. This means, that about 70 % of the probing power is reflected from the connector surface and absorbed into LED chip, the LED's PCB and the connector itself. In the case of a red LED ($\lambda = 660$ nm), only 10 % of the emitted power could be guided into the fibre.

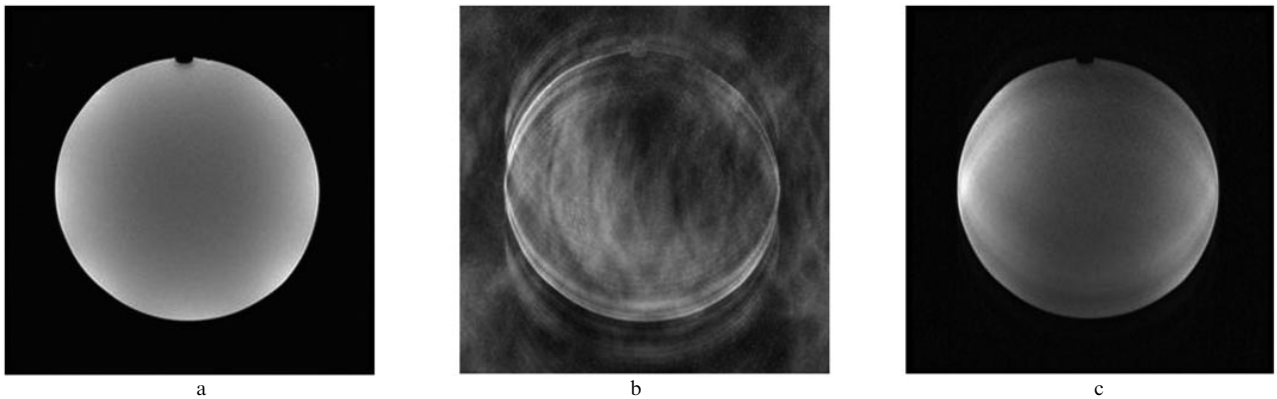

a b c

Figure 6. MR images of a calibration phantom: (a) undisturbed reference MR-image, (b) disturbed MR-image obtained during unshielded 10-channel LED driver operation, and (c) slightly disturbed MR-image during shielded 10-channel LED driver operation.

5.3 Evaluation of the setup's operating parameters by Monte Carlo simulations

To evaluate the intensity level detectable at different distances from the probing source, we performed Monte Carlo simulations of NIR reflectometry at four wavelengths, three of which corresponded to the operating wavelengths of the constructed device. Figure 7 displays the simulation results as a distance dependence of the ratio of probing to the detected power for a 10 mm^2 area of the detector.

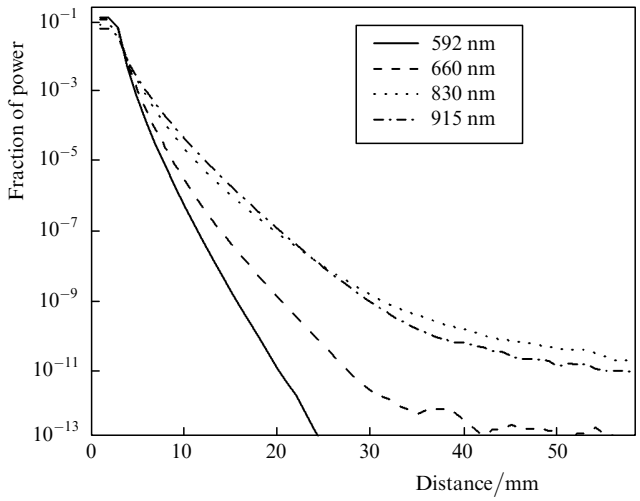

Figure 7. Fraction of the power (ratio of detected power to probing power) calculated by the Monte Carlo method for a multilayered human head model for a 10 mm^2 detector area versus source–detector separation. The probing beam was 1.5 mm in radius.

Okada et al. [13] demonstrated that to reach the grey matter layer of the brain in optical NIR reflectometry, the source–detector separation should be larger than 30 mm, otherwise the scanning depth will not exceed the total thickness of the scalp and skull layers. Obviously, these values are average, while the exact values depend on individual physiological parameters of a patient; however, they can be used for evaluation.

Results of the simulation reveal that the average detected signal level at this source–detector separation is about 8 orders of magnitude lower than at 830 and 915 nm and 11 orders of magnitude lower than at 660 nm. The signal achieved at 592 nm was obviously below the detector's threshold.

Comparison of the probing power measurements with Monte Carlo simulations results indicated that wavelength of 830 and 915 nm are sufficient for measurements in the existing configuration. The output power of the LEDs varies from 1 to 2 mW, while the detection threshold is 0.2 pW for a bandwidth of 1 mHz, which is 10 orders of magnitude lower. The measurements at 660 nm are possible after a significant increase in the output power of the LED. The power level obtained for wavelength of 592 nm is significantly lower than the detection threshold. In future, improving the noise characteristic of the detector and the amplifier should be examined.

6. Conclusions

A device for measuring blood oxygen variations by NIRS reflectometry in the MRI environment was designed, constructed, and tested for MR-compatibility. In addition, Monte Carlo simulations of light propagation in a human brain model were performed in order to evaluate signal levels at different source–detector separations. The calculations show that in the existing configuration the measurements at adult human brain can be performed employing wavelengths of 830 and 915 nm, while usage of the 660-nm wavelength requires a significant increase in the probing power; employing the wavelength of 592 nm is unpromising due to a significant probing power decay after propagation in the biotissues. The possibility of the NIRS system application for studying blood oxygen variations and metabolic fluctuations in human tissues, where the decay of probing radiation is lower than in brain, is currently considered. Clinics could utilise it noninvasively, semi-invasively or invasively during pre-operative examination or operation.

One important novelty in this device is the utilisation of the emerging high-power LED technology instead of the laser technology, which is often a costly alternative in multichannel measurements. Another novel feature is its MRI-compatibility.

Acknowledgements. The project was funded by the Academy of Finland (Grant Nos 111711 and 123772). The authors would like to thank M.Sc.(Tech.) students M. Koutonen, E. Karvonen, V. Korhonen, and M. Viteznik for their assistance when prototyping the design. E. Sergeeva and M. Kirillin acknowledge the grant of the President of the Russian Federation (MK-698.2009.2) and Federal Target Programme 'Scientific and Scientific-Pedagogical Personnel of Innovative Russia' (Project Nos 14.740.11.0253, 02.740.11.0839 and 02.740.11.0566).

References

1. Ogawa S., Lee T.M., Kay A.R., Tank D.W. *Proc. Nat. Acad. Sci.*, **87** (24), 9868 (1990).
2. Biswal B., Yetkin F.Z., Haughton V.M., Hyde J.S., *Magnetic Resonance in Medicine*, **34** (4), 537 (1995).
3. Kiviniemi V. *Human Brain Mapping*, **29** (7), 810 (2008).
4. http://omlc.ogi.edu/spectra/hemoglobin/index.html.
5. Kwon K., Park S. *Sensors and Actuators A: Phys.*, **43**, 49 (1994).
6. Vern B.A., Leheta B J., Juel V C., LaGuardia J., Graupe P., Schuette W.H. *Brain Res.*, **775**, 233 (1997).
7. Wolf M., Ferrari M., Quaresima V. *J. Biomed. Opt.*, **12** (6) 062104 (2007).
8. Myllylä T.S., Elseoud A.A., Sorvoja H.S.S., Myllylä R.A., Harja J.M., Nikkinen J., Tervonen O., Kiviniemi V. *J. Biophoton.*, DOI 10.1002/jbio.200900105 (2010).
9. Schenck J.F. *Medical Phys.*, **23** (6) 815 (1996).
10. Myllylä T., Katisko J., Harja J., Sorvoja H., Myllylä R. *Proc. Int. Symp. Medical Inform. Commun. Technol. (ISMICT)* (Oulu, Finland, 11–13 Dec., 2007) p. 4.
11. Bykov A.V., Kirillin M.Yu., Priezzhev A.V., Myllylä R. *Kvantovaya Elektron.*, **36** (12), 1125 (2006) [*Quantum Electron.*, **36** (12), 1125 (2006)].
12. Kirillin M.Yu., Bykov A.V., Priezzhev A.V., Myllylä R. *Kvantovaya Elektron.*, **38** (5), 486 (2008) [*Quantum Electron.*, **38** (5), 486 (2008)].
13. Okada E., Firbank M., Schweiger M., Arridge S.R., Cope M., Delpy D.T. *Appl. Opt.*, **36**, 21 (1997).

14. Bashkatov A.N., Genina E.A., Kochubey V.I., Tuchin V.V. *J. Phys. D: Appl. Phys.*, **38**, 2543 (2005).
15. Tuchin V.V. *Tissue Optics: Light Scattering Methods and Instruments for Medical Diagnosis* (Bellingham: SPIE Press, 2000).
16. Firbank M., Hiraoka M., Essenpreis M., Delpy D.T. *Phys. Med. Biol.*, **38**, 503 (1993).
17. Van der Zee P., Essenpreis M., Delpy D.T. *Proc. SPIE Int. Soc. Opt. Eng.*, **1888**, 454 (1993).
18. Van der Zee P. *Measurement and Modelling of the Optical Properties of Human Tissue in the Near Infrared*. PhD thesis (Univ. College, London, 1992).
19. http://sales.hamamatsu.com/assets/pdf/parts_S/S2386series.pdf.
20. Solomonson N.D., Link J.M., Krohn K.A. *Proc. 8th Workshop Targetry and Target Chem.* (Missouri, USA, June 23–26, 1999) pp 92–94.